

Optically-Boosted Planar IBC Solar Cells with Electrically-Harmless Photonic Nanocoatings

Ivan M. Santos,* Miguel Alexandre, Valentin D. Mihailetchi, José A. Silva, Tiago Mateus, Ana Mouquinho, Jenny Boane, António T. Vicente, Daniela Nunes, Ugur D. Menda, Hugo Águas, Elvira Fortunato, Rodrigo Martins, and Manuel J. Mendes*

Advanced light management via front-coated photonic nanostructures is a promising strategy to enhance photovoltaic (PV) efficiency through wave-optical light-trapping (LT) effects, avoiding the conventional texturing processes that induce the degradation of electrical performance due to increased carrier recombination. Titanium dioxide (TiO₂) honeycomb arrays with different geometry are engineered through a highly-scalable colloidal lithography method on flat crystalline silicon (c-Si) wafers and tested on standard planar c-Si interdigitated back-contact solar cells (pIBCSCs). The photonic-structured wafers achieve an optical photocurrent of 36.6 mA cm⁻², mainly due to a broad anti-reflection effect from the 693 nm thick nanostructured coatings. In contrast, the pIBCSC test devices reach 14% efficiency with 679 nm thick TiO₂ nanostructures, corresponding to a ≈30% efficiency gain relative to uncoated pIBCSCs. In addition, several designed structures show unmatched angular acceptance enhancements in efficiency (up to 63% gain) and photocurrent density (up to 68% gain). The high-performing (yet electrically harmless) LT scheme, here presented, entails an up-and-coming alternative to conventional texturing for c-Si technological improvement that can be straightforwardly integrated into the established PV industry.

1. Introduction

Wavelength-scale high-refractive index structures are among the most desirable light-trapping (LT) approaches for front surface integration on photovoltaic (PV) devices. They provide substantial anti-reflection and effective light scattering to strengthen the photocurrent generation in the absorber layer.^[1–6] Comparatively to the industrially established LT method of random micro-textured surfaces, front-located photonic coatings can yield similar (or even superior) photocurrent gains. In addition to the substantial photocurrent gains brought forth by the proposed LT approach, it avoids the harsh texturing processes that deteriorate the electrical performance of conventionally fabricated solar cells via increased charge carriers trapping or recombination.^[7] Thus, by preventing any detrimental defect density increase, the photonic structures offer a unique means to circumvent the conventional compromise between optical enhancement versus electrical deterioration that severely limits

the performance improvements attainable by texture-based LT in PV devices.^[2,8–12]

Since crystalline silicon (c-Si) is an indirect bandgap semiconductor, it benefits the most from LT schemes that act on the poorly absorbed near-infrared (NIR) photons, particularly front-located structures that lead to intense forward scattering^[2,13] such as hexagonal arrays of semi-spheroidal voids investigated in previous theoretical optimizations^[2,14] and implemented in this work. Other front structures with distinct geometries have demonstrated considerable photocurrent gains such as nature-inspired arrangements of diffractive elements with rectangular cross-sections,^[15] arrays of dielectric nano/micro-particles,^[16] or domes partially embedded in an anti-reflection coating (ARC).^[14,17] Despite the significant optical improvements reported in the literature, most investigated LT structures still lead to substantial reflection losses and low angular acceptance. These, or any other design that comprises sharp corners/edges or narrow openings (as in between the particles' base and the top cell layer), also lead to parasitic losses via thermal energy dissipation from the generated near-fields at the sharp sites. Comparatively, the LT structure employed in this work manages to circumvent

I. M. Santos, M. Alexandre, T. Mateus, A. Mouquinho, J. Boane, A. T. Vicente, D. Nunes, U. D. Menda, H. Águas, E. Fortunato, R. Martins, M. J. Mendes

CENIMAT/13N, Departamento de Ciência dos Materiais, Faculdade de Ciências e Tecnologia (FCT)

Universidade Nova de Lisboa and CEMOP/UNINOVA

2829-516 Caparica, Portugal

E-mail: imi.santos@campus.fct.unl.pt; mj.mendes@fct.unl.pt

V. D. Mihailetchi


International Solar Energy Research Center (ISC) Konstanz
Rudolf-Diesel-Str. 15, D-78467 Konstanz, Germany

J. A. Silva

Faculdade de Ciências, Universidade Nova de Lisboa (FCUL)

Instituto Dom Luiz

1749-016 Lisboa, Portugal

 The ORCID identification number(s) for the author(s) of this article can be found under <https://doi.org/10.1002/adom.202300276>

© 2023 The Authors. Advanced Optical Materials published by Wiley-VCH GmbH. This is an open access article under the terms of the Creative Commons Attribution License, which permits use, distribution and reproduction in any medium, provided the original work is properly cited.

DOI: 10.1002/adom.202300276

such issues. For instance, a theoretical photocurrent density (J_{ph}) enhancement of 48% in a 1.5 μm thick c-Si solar cell (compared to a reference cell with a flat ARC) is among the highest gains reported with semi-spheroidal void-shaped structured coatings.^[2]

In terms of optical materials, titanium dioxide (TiO_2) is an abundant (low-cost) and environmentally stable metal-oxide preferential for photonic coatings due to its relatively high real refractive index (n) part and low imaginary (k) part in the visible and NIR (vis-NIR) regions.^[13] Previous simulation and experimental works with nanostructured TiO_2 report substantial absorption enhancements on different PV absorbers (e.g., silicon or perovskite),^[1,8,9,13] owing to: 1) gradual effective refractive index matching with the high refractive index absorber ($n_{\text{TiO}_2} = 2.5 - 2.7$, $n_{\text{Si}} \approx 4$ and $n_{\text{perovskite}} \approx 2.5$); 2) light reflection diminishment at short wavelengths (UV-vis) as a result of the latter and their pyramidal-like cross-sectional shape; 3) forward light scattering of NIR photons, causing path length increase of the propagating far-field together with light focusing of the near-field generated underneath the designed structures; 4) negligible parasitic absorption in the vis-NIR regions implied by their low k .^[18,19]

Such computationally-optimized nanostructures can be fabricated by the colloidal lithography (CL) wet-coating method, as explored in this work.^[20–23] This CL technique is a low-cost soft-patterning approach that allows processing flexibility, simplicity, and precise nanostructuring over large areas.^[13,24] As it is typically performed at room temperature, it enables the patterning of temperature-sensitive materials, which is highly convenient for the large-scale fabrication of various PV technologies. Among several remarkable results, it is worth noting the pronounced >22% efficiency enhancements attained with amorphous-silicon thin-film solar cells using the CL method compared to flat reference cells.^[1,25–28]

In view of the above, we present here an advanced light-trapping approach based on photonic coatings, implemented for the first time via the CL method in wafer-based c-Si solar cells and demonstrating a cost-effective alternative to conventional random texturing. Moreover, by engineering high-index curved front nanostructures that provide a more gradual refractive index matching between the air medium and the absorber, one can achieve higher optical (hence efficiency) improvements, compared to those attained from typical micrometric textures designed through standard chemical/dry etching procedures, as reiterated in the literature.^[12,13] The photonic nanostructures were first developed and optically evaluated on flat conventional and thin (250 and 90 μm , respectively) c-Si wafers. Afterward, they were integrated into planar interdigitated back-contact solar cells (pIBCSCs, 180 μm c-Si absorber thickness). This device architecture is particularly advantageous for frontal LT schemes, since both contacts are at the bottom of the cell, thus leaving the top Si surface fully exposed to the impinging light.

A multiparameter analysis of the LT integration process was also performed to maximize the photocurrent density and efficiency. Each step of the CL method is addressed in the next section, followed by the morphological and optical characterization of the wafers endowed with nanostructured coatings and lastly the optical and electrical response of the pIBCSCs. The results demonstrate a remarkable increase in the optoelectronic performance (i.e., absorption and efficiency) of the tested cells, which, together with the proven scalability of the CL technique, reveals

a simple, industrial-friendly, and versatile approach to boost the power generation of commercial PV devices.

2. Results

2.1. Colloidal-Lithographed Crystalline Silicon Wafers

The CL procedure applied in this work involves the four main steps described below and further detailed in previous contributions of the authors.^[25,29] The first step consists in depositing a self-assembled and highly-ordered close-packed monolayer (acting as the lithographic mask) of colloidal polystyrene microspheres (1.3 μm diameter) through Langmuir-Blodgett (LB) on the surface of the sample. **Figure 1a** shows a conventional silicon wafer covered with the resultant colloidal mask, which highlights the remarkable long-range ordering achieved with such a simple wet-patterning process over large areas, as well as its scalability since the coverable area is only limited by the dimensions of the used LB tank and trough. The resulting array of spheres was assessed by scanning electron microscopy (SEM) post-image processing with fast Fourier transform (FFT). The FFT image in the inset of **Figure 1b** shows a highly adequate medium-range order, identified by the four distinct rings with defined peaks, which correspond to an intermediate case between perfectly ordered (intense and well-defined peaks in a honeycomb array) and a poor arrangement (fading concentric rings without defined peaks).

In the next step, the spheres are downsized and shaped through a selective O_2 reactive ion etching (RIE) process, which was applied for 100–400 s in this work. Per se, longer O_2 RIE times (t_{RIE}) result in higher inter-particle spacing, as depicted in **Figure 1c,d** with SEM images taken after the entire CL process. Since the etching is mainly perpendicular to the surface, the spheres experience an anisotropic modification of their shape from spheres to spheroids, following a geometric model detailed in the literature.^[30] Such exposure to the RIE environment also increases the surface roughness of the particles, as observed in this work for O_2 $t_{\text{RIE}} \geq 300$ s. This can distantiate the geometry of the final structures from the intended smooth curvature of the designed voids simulated in related works,^[3,14] and thus, from the optimal interaction with light. Nevertheless, their periodicity and center-to-center distance (pitch) are retained throughout the RIE process. Third, the non-closed-packed array, created by the inter-particle spacing produced by RIE exposure, is filled with TiO_2 deposited by radio-frequency (RF) sputtering. The longer the deposition, the thicker the resulting TiO_2 features will be. However, since the deposited material accumulates both on the masking particles and on their interspace, the maximum aspect ratio of the features that can be reached is limited by the size of the spheres.^[1,9] As assessed in previous works, the maximum height that can be attained for the designed voids through this CL method is close to the radius of the initial spheres (in this case, 650 nm).

The fourth and last step comprises the lift-off of the colloidal mask. First, a second RIE (under $\text{Ar} + \text{CF}_4$ atmosphere) is applied to remove the TiO_2 top layer capping the particles. Then, a toluene sonication bath chemically dissolves the polystyrene material of the colloids, leaving only the TiO_2 photonic nanostructured coating.^[13,25] In **Figure 1c,d**, some undesirable

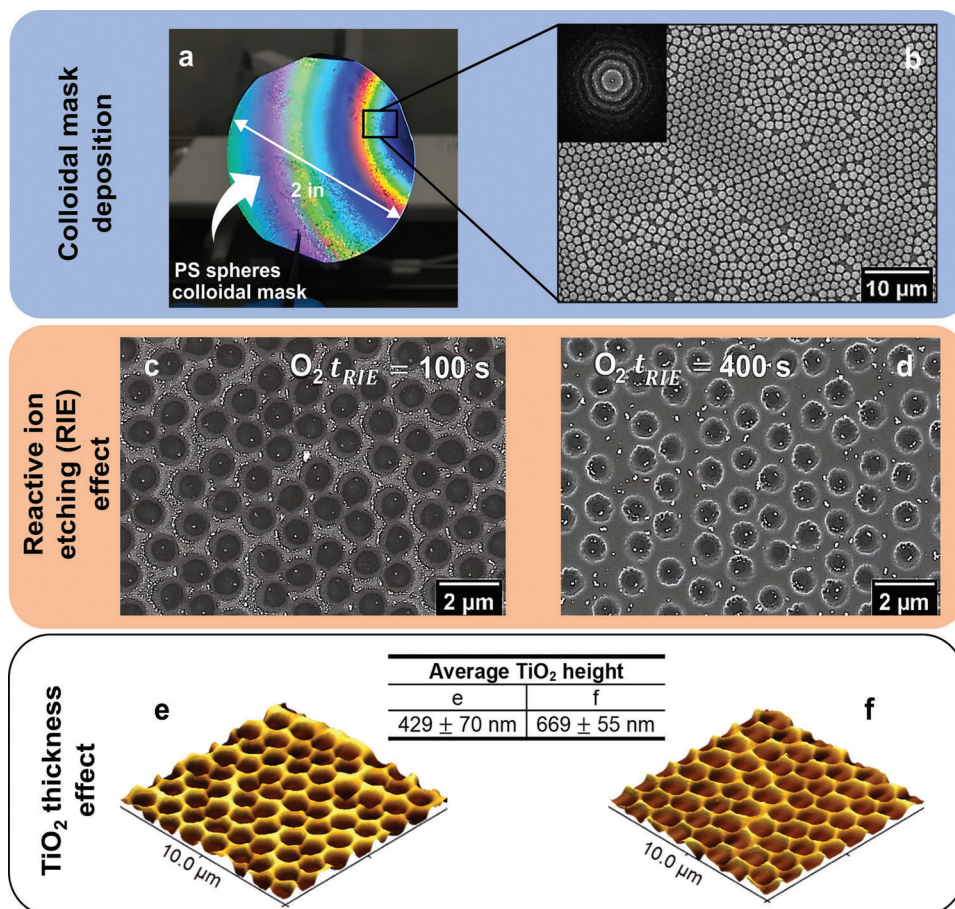


Figure 1. Morphological and topographical assessment of photonic nanostructured coatings on c-Si wafers. a) Digital photograph of a 2-in. diameter wafer covered with a close-packed colloidal mask of 1.3- μm diameter polystyrene (PS) particles deposited in the first Langmuir Blodgett (LB) step. b) Corresponding SEM top-view and inset showing the Fast-Fourier Transform graphical representation. c,d) SEM top-views of the resulting TiO₂ nanostructures (275 \pm 15 nm thick) employing c) 100 and d) 400 s of O₂ reactive ion etching (RIE). e,f) 3D orthographic projection of 10 \times 10 μm^2 AFM top-views of two nanostructured coatings on c-Si wafers, resultant of 300 s of O₂ RIE time. The average TiO₂ heights are 429 \pm 70 nm (equivalent film thickness of 430 nm deposited by sputtering) and 669 \pm 55 nm (equivalent film thickness of 792 nm), respectively.

polystyrene residues (bright fragments) can be observed, suggesting a shorter-than-required lift-off time. Nevertheless, the optical performance within the wavelength range of interest (350–1400 nm) is not affected by these residues.^[29]

The main parameters of the CL process investigated in this work and their effects on the final structures are listed in the Experimental Section. To design high-aspect ratio features, the deposited TiO₂ thickness was kept relatively close to the initial radius of the colloids, as shown by the topography of two representative nanostructured coatings on conventional flat (double-side polished) silicon wafers presented in Figure 1e,f. Besides confirming the arrangement of the designed features, it is possible to correlate the average height of the structures (see Figure S1, Supporting Information, for more details) with the equivalent TiO₂ film thickness deposited. The average height of the features in Figure 1e matches the equivalent film thickness since the deposited material thickness is inferior to the radius of the masking colloids. Contrastingly, in Figure 1f, the equivalent thickness is well above the colloid radius, meaning that a significant portion of the deposited TiO₂ was removed during the final lift-off step.

The optical performance of the nanostructured coatings was first assessed on double-side polished c-Si wafers (conventional 250 μm , and thin 90 μm) with an Ag rear layer acting as a back mirror. The performance was evaluated via spectrophotometry by determining the spectrally-averaged absorption, $\langle Abs \rangle$, and the optical photocurrent density, J_{ph} , computed by convolution of the absorption with the solar irradiance (AM1.5) spectra. In addition to the intense forward-scattering effect for longer NIR wavelengths (NIR, \geq 800 nm, depicted by the red arrows in Figure 2), the designed coatings also result in a broad light in-coupling effect, as illustrated in Figure 3a. The combination of the pyramidal-like cross-sectional shape with the high real part of the TiO₂ refractive index ($n \approx 2.5 - 2.7$) provides a geometrical and gradual effective index matching between the air ($n \approx 1$) and the absorber ($n \approx 4$), as illustrated in Figure 2. In other words, it induces a higher and broader wave-impedance matching with the impinging light which, in turn, leads to a spectrally-wide reflection reduction (across the UV–vis–NIR).^[9,13] According to simulation and experimental works,^[9,14] the highest anti-reflection effect in UV–vis should be reached with the highest aspect ratio

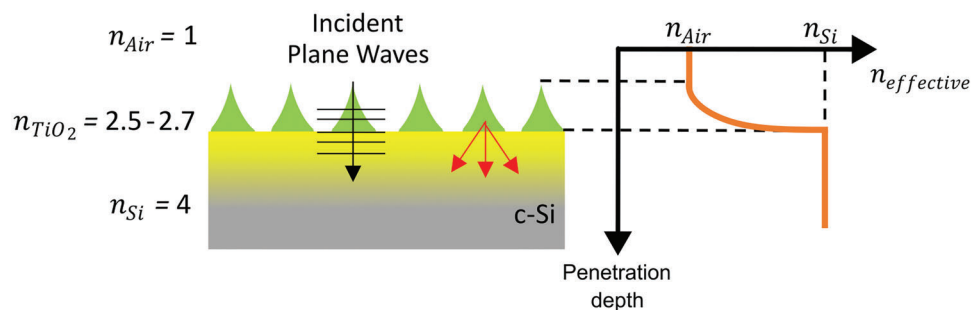


Figure 2. Sketch of the geometric index matching plus the scattering effects caused by the wave-optical front light-trapping structures. The increasing cross-sectional area of the TiO_2 features, with respect to the incidence direction, provides a smooth transition for the effective index (n) experienced by the impinging light. Moreover, the high TiO_2 index and wavelength-scale dimensions of the front features enable strong scattering of the in-coupled photons toward the crystalline-silicon (c-Si) absorber (red arrows), hence resulting in a higher and more uniform spatial distribution of light absorption across the c-Si volume (yellow gradient).

features. This is corroborated mainly in the visible band, as observed in the transmittance and reflection spectra for both c-Si wafer thicknesses presented in Supporting Information (Figure S2a–d, Supporting Information).

When accounting for the full solar spectrum, the highest attained J_{ph} (see Equation (1) in the Experimental Section) were 36.6 and 35.6 mA cm^{-2} for the conventional and thin wafers, respectively, with the following t_{RIE} and TiO_2 infiltration thickness combination: 300 s and 669 nm, and 350 s and 693 nm (average TiO_2 thickness), as shown in Figure 3c,d. These results are mainly due to the broad and more intense anti-reflection effect obtained for these conditions. It is important to note that the determined photocurrent density incorporates any parasitic absorption within the photonic coatings, which chiefly occurs in the UV band, as TiO_2 presents a significant k in that range ($\approx 2.5 - 3.5$ for 300–400 nm wavelengths).

The optical performance of the designed coatings was compared to that of an optimized single-layer (planar) anti-reflection coating (pARC, ≈ 50 nm thick TiO_2). The pARC induces a strong anti-reflection effect between 600 and 1000 nm, with a maximum of around 600 nm, as revealed in Figure 3e,f for both types of wafers. However, this effect is spectrally narrower than that attained with the best-performing nanostructured LT coatings, which is confirmed by their superior $\langle \text{Abs} \rangle$ (insets of Figure 3e,f). Moreover, a significant scattering effect in the NIR band is attained with the nanostructures, contrary to the planar films. Therefore, the CL-fabricated LT designs led to higher J_{ph} values than those attained with the pARC (34.9 and 33.2 mA cm^{-1} , respectively, for 250 and 90 μm c-Si wafers), as verified in Figure 3g,h.

The optical gains achieved by applying the nanostructured coatings are higher for lower absorber material thicknesses (see the $\langle \text{Abs} \rangle$ and J_{ph} enhancements in Table 1).^[8,13] Nevertheless, non-negligible broad reflection losses still leave room for improvement toward the classical $4n^2$ Lambertian limit (corresponding to 43.7 and 42.5 mA cm^{-2} , respectively).^[9,31,32] Yet, it is noteworthy that for longer NIR wavelengths (>1150 nm) the absorption attained with the photonic nanostructured coatings surpasses this limit, as a result of interference effects that are not accounted for in the geometric ray optics regime of the Lambertian formalism. The best-performing coatings engineered in this work reached 83.8% of this theoretical LT limit. Reported ex-

perimental work for flat c-Si wafer thicknesses between 20 and 190 μm was closer to the Lambertian ideal case (99.8% of the ideal J_{ph}) when using nanotexturing processes on both front and rear surfaces.^[33,34] However, on electrical grounds, these plasma dry etched textures in c-Si are disadvantageous, as they can largely increase the defect density of the active region. Such drawback is circumvented with the CL-patterned top coatings here developed since they avoid structuring the PV layers while providing strong LT. Also, our method can be applied to a wide range of PV absorbers, not being limited solely to c-Si.^[1,28,29,35]

2.2. Photonic-Enhanced Planar Interdigitated Back-Contact Solar Cells

The developed LT structures were then applied on pIBCSCs with a standard 180 μm thick c-Si absorber. The as-fabricated pIBCSCs used in this work as test bed were constructed with double-side polished c-Si wafers intended to be as planar as possible. Still, they present a subtle microscale roughness, as shown in the inset of Figure 4a, with relatively wide in-plane dimensions on the order of 100 μm . However, such roughness does not significantly affect the CL patterning of the nano-voids array or the measured optical properties of the devices, as confirmed by the authors.

For the cell patterning, the t_{RIE} was maintained at 300 s, while the deposited TiO_2 film thickness was varied between 281 and 705 nm, being the latter the highest thickness that ensured high-quality and high-aspect ratio features with the 1.3 μm diameter masking spheres used in the CL process. The presented results focus on the taller arrays, which were expected to yield better optical performances, considering the results in the previous subsection. Figure 4a depicts a tilted SEM view of the best-performing TiO_2 nanostructure on top of a pIBCSC. The CL method gave rise to a long-range ordered honeycomb array covering the planar surface homogeneously.

The application of the photonic coatings led to the combination of the following effects: light scattering and increased optical path length of long-wavelength photons (>900 nm), together with broad anti-reflection mainly of the shorter-wavelength photons (see Figure S2e,f, Supporting Information, namely transmittance and reflectance spectra). These effects led to a broad absorption enhancement in the wavelength range of study (350–1200 nm),

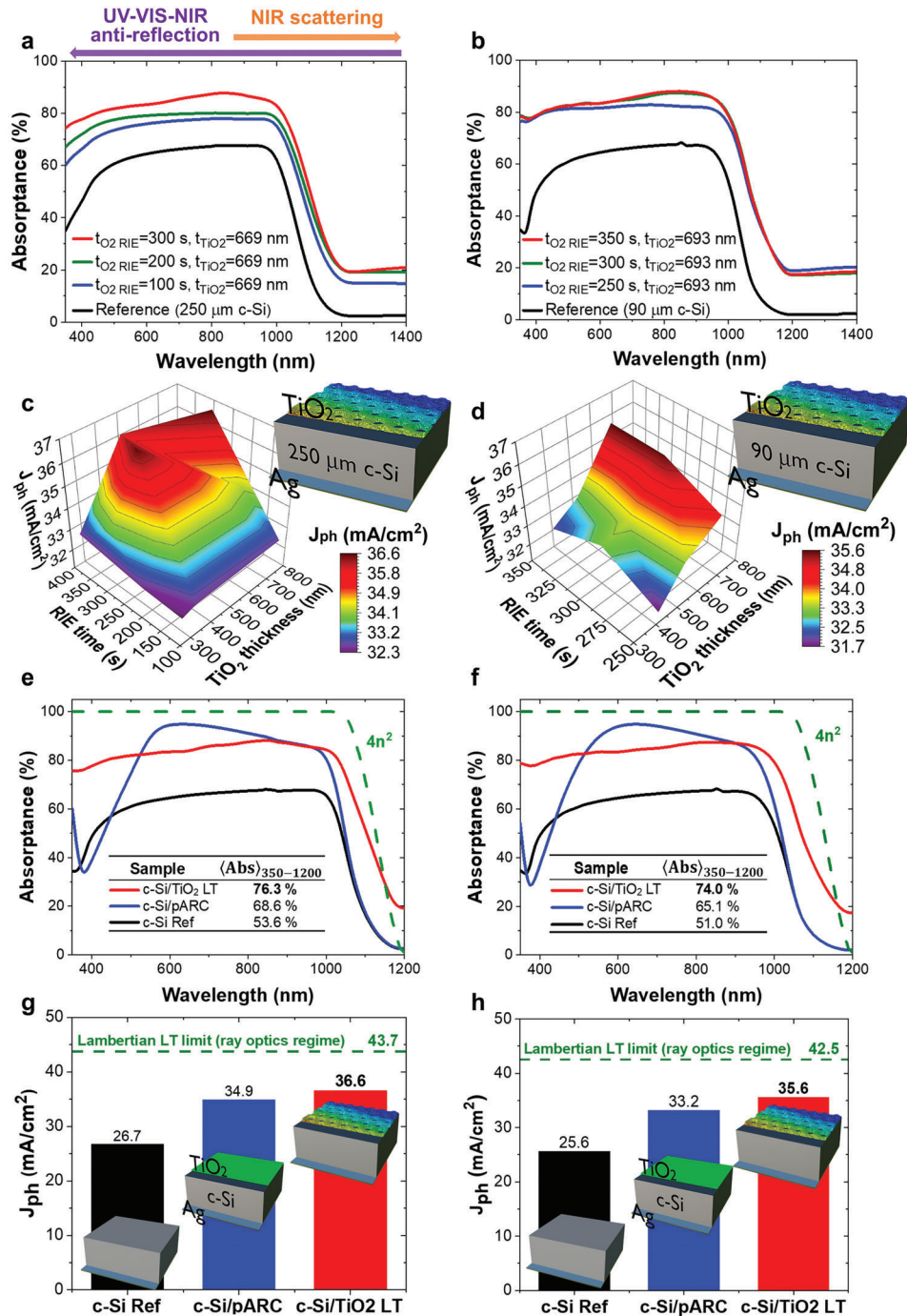


Figure 3. Optical assessment of photonic nanostructured coatings on conventional (250 μm, left side – plots a, c, e, g) and thin (90 μm, right side – plots b, d, f, h) double-side polished c-Si wafers having a 300 nm Ag mirror at the rear. a,b) Measured absorbance spectra of representative batches of c-Si wafers coated with TiO₂ features with the different O₂ t_{RIE} and thicknesses (t_{TiO_2}) presented in the inset table, where the 300 s green curve in (b) is mostly covered by the 350 s red curve. The references comprise uncoated wafers with the Ag rear mirror. c,d) 3D plots showing J_{ph} as a function of O₂ t_{RIE} and TiO₂ thickness of the designed coatings. e,f) Absorbance spectra of the uncoated wafer (c-Si Ref), coated with optimized planar anti-reflection coating (≈ 50 nm TiO₂, c-Si/pARC) and best-performing samples with photonic nanostructured coatings (c-Si/TiO₂ LT, corresponding, respectively, to 669 nm TiO₂, O₂ t_{RIE} = 300 s and 693 nm TiO₂, O₂ t_{RIE} = 350 s). The “4n²” spectra correspond to the theoretical ideal absorption in Lambertian formalism. g,h) Spectrally integrated (350–1200 nm) absorbance, presented regarding J_{ph} for the samples of (e) and (f), respectively. The determined J_{ph} of the theoretical Lambertian limit (for 250 and 90 μm of c-Si) is marked with a horizontal dashed line.

Table 1. Maximum $\langle Abs \rangle$ and J_{ph} values (determined in the 350–1200 nm wavelength range) attained for planar c-Si wafers, with thickness t_{wafer} and the best-performing nanostructured coatings applied on top.

t_{wafer} [μm]	Best-performing wave-optical LT structure					Lambertian LT limit		
	$\langle Abs \rangle$	$\Delta_{\langle Abs \rangle}$	J_{ph} [mA cm^{-2}]	$\Delta_{J_{ph}}$	J_{ph}^{ARC} [mA cm^{-2}]	$\Delta_{J_{ph}^{ARC}}$	$J_{ph}^{Lamb.}$ [mA cm^{-2}]	$J_{ph}/J_{ph}^{Lamb.}$ [%]
250	76%	42%	36.6	37%	34.9	5%	43.7	84%
90	74%	45%	35.6	39%	33.2	7%	42.5	

The CL patterning parameters are respectively the following (TiO_2 thickness and O_2 t_{RIE}): 669 nm and 300 s (for the 250 μm wafer), 693 nm and 350 s (90 μm wafer). The enhancements were calculated against the uncoated reference wafer ($\Delta_{\langle Abs \rangle}$ and $\Delta_{J_{ph}}$) and a wafer coated with an optimized anti-reflection coating ($\Delta_{J_{ph}^{ARC}}$) made of a single flat TiO_2 layer. The results are also compared to the ideal Lambertian LT limits analytically computed in the regime of geometrical optics. t_{wafer} , wafer thickness; $\langle Abs \rangle$, average absorption; $\Delta_{\langle Abs \rangle}$, enhancement of average absorption; J_{ph} , photocurrent density; $\Delta_{J_{ph}}$, photocurrent density enhancement; ARC, Anti-reflection coating; *Lamb.*, Lambertian.

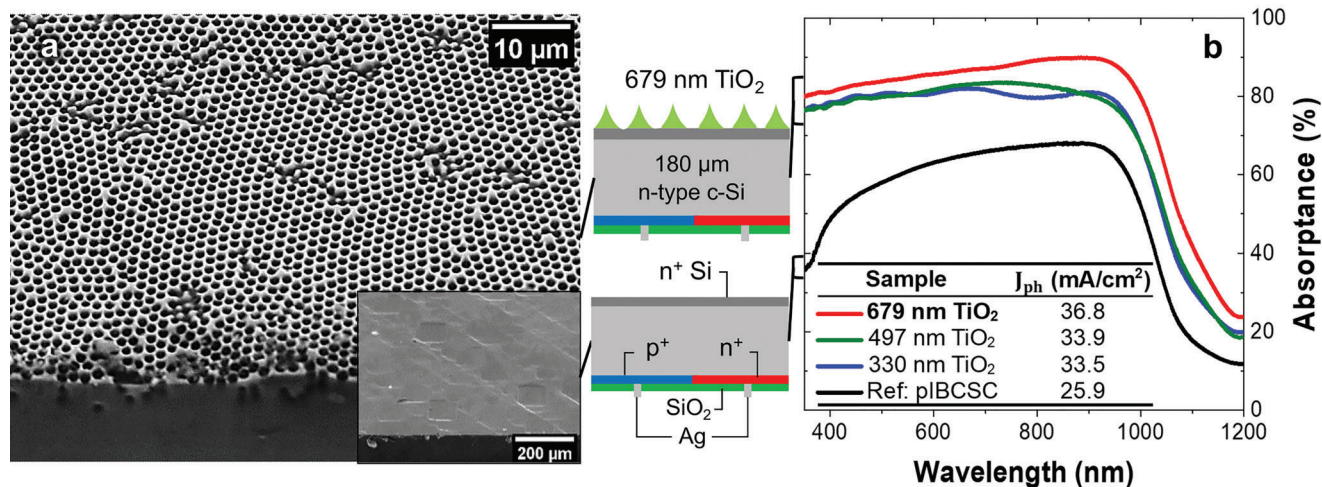


Figure 4. Morphological and optical assessment of planar interdigitated back contact solar cells (pIBCSCs) endowed with photonic coatings. a) SEM tilted-view (45°) of pIBCSC (180 μm of c-Si absorber) covered with a nanostructured coating (679 nm TiO_2 , O_2 $t_{\text{RIE}} = 350$ s). The inset shows the uncoated as-fabricated pIBCSC with microscale roughness. b) Absorbance spectra of pIBCSCs coated with photonic nanostructures (see top sketch) CL-fabricated with $t_{\text{RIE}} = 300$ s and different TiO_2 thicknesses: 330, 497, and 679 nm. These are compared to the pIBCSC reference (black), whose device architecture is depicted in the bottom sketch. The inset table shows the optical J_{ph} determined by integrating the absorption spectra between 350 and 1200 nm.

which corresponds to the “useful” absorption in the c-Si material. The 705 nm TiO_2 coating composed of the taller features reached 36.8 mA cm^{-2} of J_{ph} in the selected range (see table within Figure 4), which corresponds to a $\approx 43\%$ gain relative to the $J_{ph} = 25.8 \text{ mA cm}^{-2}$ of the uncoated reference pIBCSC.

The corresponding J – V curves are presented in Figure 5a and compared with the uncoated pIBCSC reference. The LT-induced absorbance gains translated in the enhancement of 1) short-circuit current density (J_{sc}) and 2) broadband external quantum efficiency (EQE) in the considered range for TiO_2 thicknesses ≥ 505 nm. The photocurrent gains originated by these structures are perceptible when analyzing their EQE spectra (see Figure 5b,c). Particularly for the longer wavelengths (>900 nm), where both anti-reflection and light scattering effects compound, the relative EQE enhancement reaches more than 150% for the 705 nm TiO_2 features. In the table in Figure 5, it is seen the open-circuit voltage (V_{oc}) barely reduced with the inclusion of the photonic coatings relative to the pIBCSC reference, showing that they are electrically harmless. These results demonstrate the potential of the developed LT structures to improve the full optoelectrical performance of the PV devices, maximizing, respectively, the J_{sc}

and power conversion efficiency (PCE) gains up to 28% and 30% are attained with the thickest coating (705 nm TiO_2). This mismatch between both gains is due to the slight V_{oc} and fill factor (FF) increases attained with TiO_2 coatings thicker than 505 nm, as depicted in Figure 5c.

For practical applications, it is crucial to evaluate the response of the solar cells under oblique incidence, as they can operate without sun-tracking mechanisms. The angle-resolved electrical performance of the cells was measured for incidence angles from 0° (normal to the cell surface) to 90° (parallel to the surface), and the corresponding evolution of the J – V curves is shown in Figure 6a for the best-performing samples (497 and 679 nm of TiO_2). As expected, the reflection losses increase with the incidence angle, thus the power output is reduced. The dependence of V_{oc} , J_{sc} , FF, and PCE with the incidence angle is depicted in Figure 6b. The enhancements regarding PCE and J_{sc} are shown in Figure 6c, determined relative to the uncoated pIBCSC (reference). Although the V_{oc} and FF of the coated pIBCSCs are unaffected by the angle variation, as shown by the similar trends of the coated and uncoated planar cells (Figure 6c), the application of the TiO_2 structures led to superior J_{sc} (hence also efficiency).

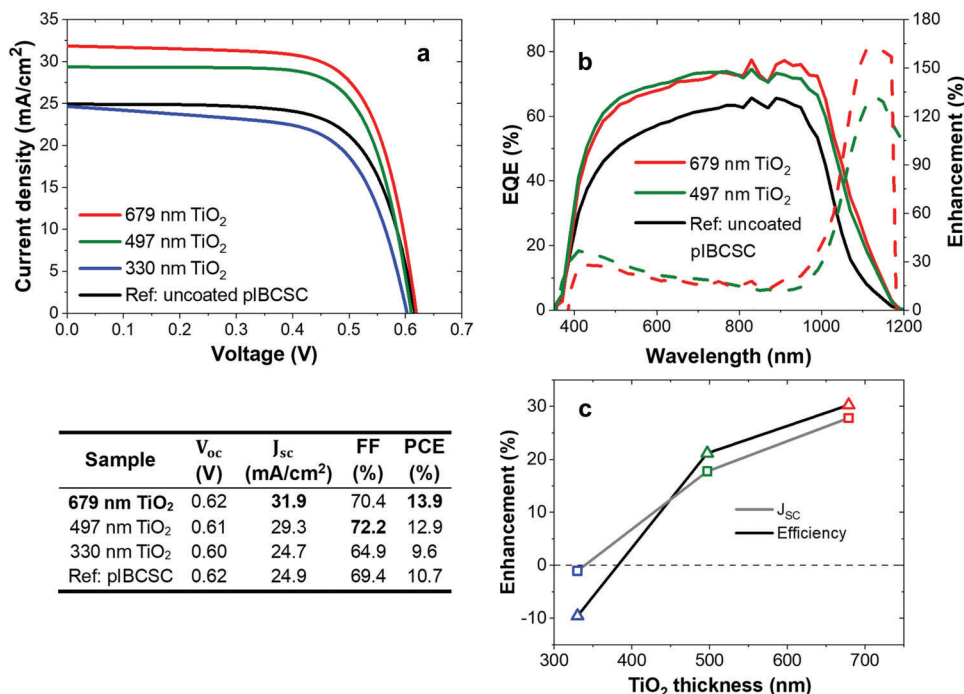


Figure 5. Electrical assessment of pIBCSC endowed with photonic coatings. a) J - V curves of the pIBCSC coated with 330 nm (green), 497 nm (blue), and 679 nm (red) thick TiO₂ nanostructures, compared with the J - V of the uncoated reference. b) External quantum efficiency (EQE) spectra obtained for the best-performing TiO₂ thicknesses of 497 and 679 nm. The colored lines correspond to the coated solar cells, whose enhancements (in dashed lines) are determined against the uncoated pIBCSC (in black). The corresponding cell characteristics, that is, open-circuit voltage (V_{oc}), short-circuit current density (J_{sc}), and power conversion efficiency (PCE), are presented in the table (bottom left). c) Corresponding PCE and J_{sc} enhancements determined with respect to the pIBCSC reference.

Figure 6 also reveals that the LT coatings are even more beneficial for oblique illumination. Both J_{sc} and PCE present a similar growth with the increase of incidence angle: the gains for 497 nm TiO₂ reached 58% and 63%, respectively, in J_{sc} and PCE, while with a 679 nm TiO₂ LT structure the improvements were 68% and 33%, correspondingly. This is due to the outstanding angular acceptance of light provided by the curved nanostructured voids, contrastingly to the reference pIBCSCs with a flat front surface.^[3,13,14]

To the authors' knowledge, the results shown in this work are among the highest LT-induced efficiency improvements reported. The application of similar front photonic structures has been tested on other types of solar cells, namely wafer-based (e.g., GaAs by Yu et al.)^[36] and thin-film devices (e.g., a-Si:H by Sanchez-Sobrado et al.)^[1] The former study reports high short-current density improvements ($\approx 53\%$) relative to those attained here ($\approx 28\%$), but on quantum-well solar cells with ultrathin absorbers (1.5 μm). The thinner the absorber the higher can be the J_{sc} gains with effective LT in place.^[13] On the other hand, the work of Sanchez-Sobrado et al.^[1] is relevant to compare the performance under oblique light incidence. In this latter study, similar IZO nanostructures were CL-engineered on optimized IZO contacts, reaching a maximum photocurrent gain of $\approx 53\%$ with a light incidence angle of 70° when compared to unpatterned solar cells. This enhancement is surpassed in the present work with TiO₂ nanostructures, which yield $\approx 68\%$ of maximum photocurrent improvement at an 80° incidence angle. Moreover, greater enhancements are also attained here even under normal

incidence, where $\approx 30\%$ of efficiency gain is achieved, versus the $\approx 23\%$ gain reached by Sanchez-Sobrado et al.

3. Conclusion

A successful and easily-scalable colloidal lithography method is presented as a flexible gateway for light management in wafer-based c-Si photovoltaic technology.^[1,18,30,31] Through the application of the described high-index TiO₂ nanostructured coatings, unprecedented levels of broadband light-trapping (hence absorption enhancement) can be achieved for conventional and thin flat c-Si wafers, as well as for planar interdigitated back contact solar cells.

When optically evaluating the c-Si wafers coated with the photonic nanostructures, the integrated absorbance spectrum convoluted with the solar photon flux resulted in photocurrent density (J_{ph}) values of 36.6 (250 μm c-Si) and 35.6 mA cm⁻² (90 μm c-Si), respectively, for the following conditions: 300 s of RIE time (t_{RIE}) and 669 nm of TiO₂ coating; and $t_{RIE} = 350$ s and 693 nm of TiO₂. These correspond respectively to 5% and 7% of J_{ph} gain, relative to the optimized planar single-layer ARCs, with the highest enhancement being at 83.8% of the ideal J_{ph} for the theoretical Lambertian light-trapping limit. On the other hand, it is noteworthy the substantial photocurrent gains (up to 43% relative to uncoated reference cells) attained here with thick (180 μm) silicon absorbers, as compared to the theoretically-optimized 48% photocurrent gain reported in the literature with ultrathin (1.5 μm)

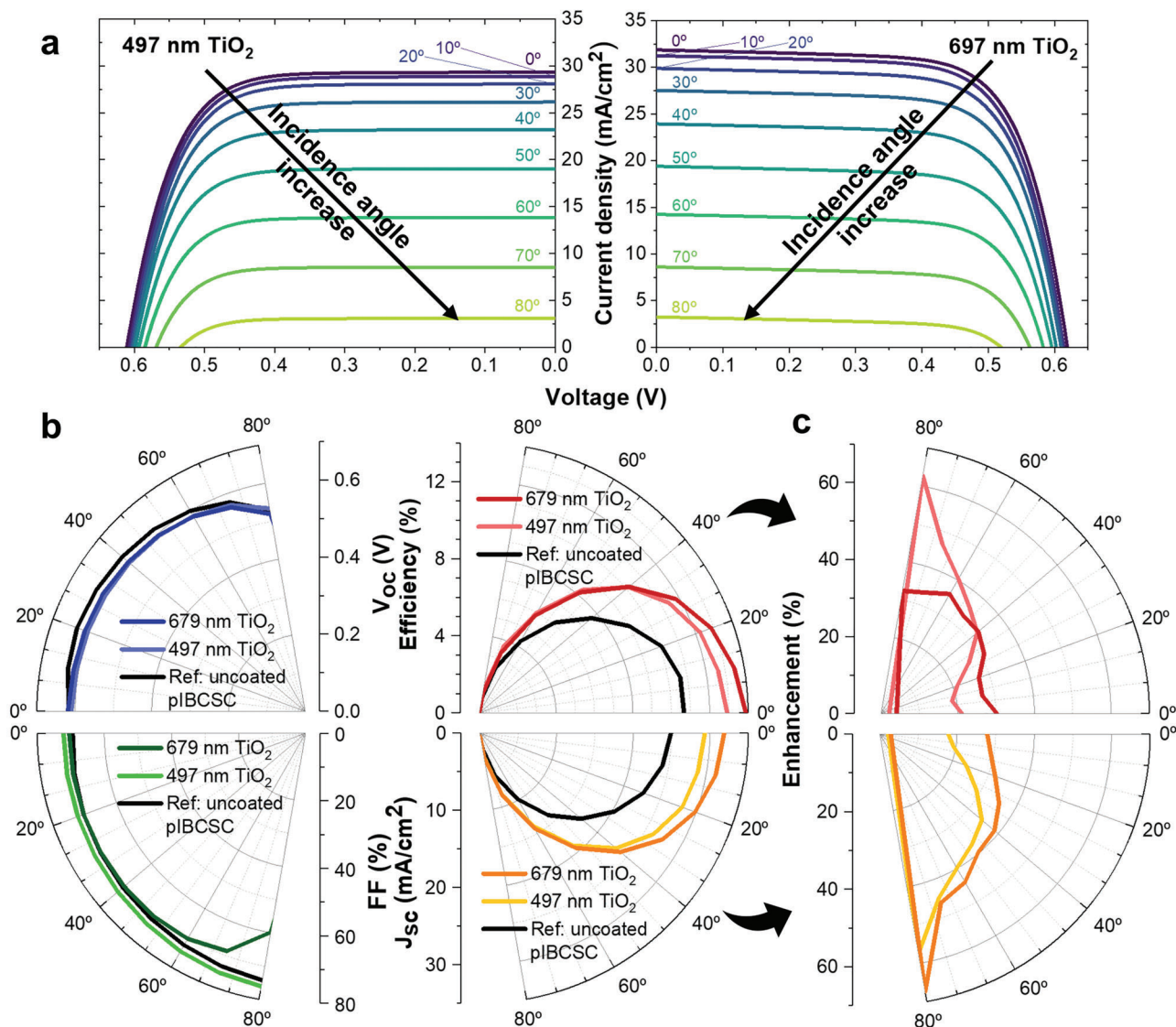


Figure 6. Angular response of the photonic-enhanced pIBCSCs. a) J - V curves of the pIBCSC covered with TiO₂ photonic nanostructures with 497 (left) and 679 nm (right), showing the evolution with the incidence angle from 0° (light impinging normal to the surface) to 80°, with a 10° step. b) Polar plots presenting the angular dependence of V_{oc} (in blue), FF (green), efficiency (red) and J_{sc} (orange). c) Efficiency (top) and J_{sc} (bottom) enhancement, determined with respect to the response of the uncoated pIBCSC reference (black in (b)).

ones,^[2,14] forecasting the application of the here designed photonic nanostructures over a wide range of absorbers thicknesses.

Regarding the coated pIBCSC devices, there were significant optical improvements without diminishing the original electrical performance. The absorption enhancement was maximum for the thickest nanostructures (679 nm TiO₂) due to greater broad anti-reflection (mainly for wavelengths <900 nm) and light scattering (900–1200 nm) effects, rendered by the high-index wavelength-sized features with high aspect ratio. It resulted in outstanding gains in J_{sc} (up to 28%) and PCE (up to 30%), attained for TiO₂ thicknesses ≥ 497 nm, which are among the highest LT-induced enhancements reported thus far for wafer-based c-Si photovoltaics. Moreover, in this work, unmatched angular performance enhancements were shown for high incidence an-

gles; particularly at 80°, the PCE and J_{sc} increased by 33% and 68%, respectively, for the 679 nm of nanostructured TiO₂.

Overall, this study unveils a highly promising alternative to the standard electrically-harmful surface texturing of c-Si solar cells through electrically-harmless photonic nanostructured coatings that allow strong LT. This solution can be implemented as a post-process on the front of completed devices, thus enabling straightforward integration in the established PV industry.

4. Experimental Section

Interdigitated Back-Contact Solar Cells Fabrication: The IBCSC architecture used in this study was based on ISC Konstanz's ZEBRA cell technology.^[37] These cells were fabricated on Cz-Si n-type wafers with a

Table 2. Experimental conditions of the two distinct dry etching (RIE) procedures.

RIE gas	Etched Material	Time [s]	RIE Power [W]	Gas pressure [mTorr]	Gas flow [sccm]	Effect
O ₂	Polystyrene	100–400	50	50	50	Inter-particle spacing for TiO ₂ infiltration.
Ar/CF ₄	TiO ₂	90	100	100	4/16	Capping layer removal for lift-off.

Table 3. Experimental conditions of the radio-frequency (RF) sputtering deposition (infiltration) of TiO₂.

Target specifications	Ar gas pressure [mbar]	Power [W]	Deposition rate [nm min ⁻¹]	Distance to sample [cm]	Pre-sputtering time [min]
TiO ₂ 99.99% purity, 3" diameter	2 × 10 ⁻³	200	2.5	15	15

base resistivity of $5 \pm 1 \Omega \text{ cm}$ and a thickness of $180 \pm 10 \mu\text{m}$. Prior to the diffusion processes, all wafers underwent an alkaline saw-damage etching followed by piranha cleaning. The p⁺ (boron) emitter, as well as n⁺ (phosphorous), front and back-surface field (FSF/BSF) diffused regions were formed, one after the other, in a quartz tube furnace containing either BBr₃ or POCl₃ gas. The sheet resistance of the emitter and the FSF region was $150 \pm 10 \Omega \text{ sq}^{-1}$, whereas the BSF region was about $80 \pm 10 \Omega \text{ sq}^{-1}$. The patterning of the rear side, to form the interdigitated n⁺ and p⁺ structures, was formed by laser ablation of a SiN_x masking layer. The passivation of the diffused regions was achieved by a stack of thermal SiO₂/SiN_x. For this study, all IBC cells were fabricated with planar (alkaline polished) front and rear surfaces. The metallization was applied using a method of screen printing and firing process from ZEBRA technology.^[37] Following the metallization process, the SiO₂/SiN_x passivation stack on the front side of the cells was removed in an HF solution to apply the photonic nanostructures developed in this study. Several of these pIBCSCs with an area of $20.9 \times 20.9 \text{ mm}^2$ were fabricated on a single M2 wafer and subsequently separated into individual cells at the end by laser cutting.

Preparation: The pIBCSCs, and conventional and thin c-Si double-side polished wafers ($250 \pm 25 \mu\text{m}$ and $90 \pm 10 \mu\text{m}$ of thickness, respectively) with corresponding diameters of 2 and 4 in. from Siltronic, were cut and submitted to 15 min of ultrasonication in isopropyl alcohol. After water and ethanol rinsing, these were dried under a nitrogen flow.

To engineer the photonic nanostructured coatings, a soft-lithography method was used, similar to related works^[1,9,29] and briefly explained below.

Polystyrene Suspension Preparation: A 10% colloidal suspension of polystyrene spheres with a diameter of $1.30 \pm 0.03 \mu\text{m}$ (which defines the pitch of the array) was purchased from Microparticles GmbH and diluted into a diacetone solution containing 1% styrene and 0.1% sulfuric acid in a ratio of 1:1, similarly to the procedure introduced by Akinoglu et al.^[30]

Langmuir–Blodgett and Fast Fourier Transform: Before filling the Biolin Scientific KSV NIMA controllable LB setup to wet-coat the colloidal monolayer, it was cleaned using deionized water followed by ethanol. The LB tank was then slightly overfilled with 700 mL of deionized water that sealed the air–liquid interface. A laboratory aspirator was then used to remove impurities on the interface.

Approximately 400 μL of the prepared solution was placed directly in the air–liquid interface with a microsyringe. The barriers of the LB setup were closed at 5 mm min^{-1} , which assembled the floating spheres in a close-packed hexagonal array, formed at the air–liquid surface. Next, the complete transfer of the formed monolayer to the surface of the samples was performed by dip-coating at a withdrawal speed of 4 mm min^{-1} . The trough withdrawal speed matched the barriers compression speed to preserve the monolayer arrangement.

The resultant spheres arrangement was assessed by processing SEM images with FFT, calculated in the software ImageJ. Briefly, this allowed as-

sessing the arrangement periodicity of the deposited particles through the number of distinct rings, or the so-called peaks (bright dots), observable in the computed FFT greyscale image. A higher number of well-defined concentric peaks correspond to a longer-order periodicity.

Colloidal Mask Shaping and TiO₂ Infiltration: Using a Trion Phantom 3 reactive ion etcher, the geometry of the spheres was tuned by O₂ RIE exposure, with the conditions listed in Table 2. TiO₂ was deposited via radio frequency magnetron sputtering (see Table 3). Glass samples with $2.5 \times 2.5 \text{ cm}^2$ also accompanied every deposition to evaluate the TiO₂ film thickness, as described below (see “Optical Assessment,” Experimental Section).

Colloidal Mask Lift-Off: A second RIE treatment under an Ar/CF₄ gas mixture (Table 2) was employed to remove the top capping layer of TiO₂ to expose the polystyrene colloids and then dissolve them by a chemical attack in a toluene sonication bath for 1 h.

Ag Rear Mirror Deposition: Silver rear mirrors ($\approx 300 \text{ nm Ag}$) were deposited via resistive thermal evaporation on the prepared c-Si wafers at a deposition rate of 0.3 nm s^{-1} . The deposited Ag thickness was confirmed by profilometry using a Dektak 3 Profilometer.

Scanning Electron Microscopy and Atomic Force Microscopy: The morphology of the samples was analyzed by top/tilted views with a Hitachi Regulus SU8220 SEM equipment. Selected SEM images were processed to obtain the aforementioned FFT images. The corresponding topographies were revealed by atomic force microscopy (AFM) using an Asylum MFP3D system.

Optical Assessment: A UV–vis–NIR spectrophotometer (PERKIN ELMER Lambda 950), comprising a 15 cm diameter integrating sphere, was used to acquire the total (T_T) and diffuse (T_D) transmittance and also the total (R_T) and diffuse (R_D) reflectance spectra of the prepared wafers and pIBCSCs in the 350–1400 nm wavelength range. The total absorbance (A_T) of the samples was determined using the following formula: $A_T (\%) = 100\% - T_T (\%) - R_T (\%)$.

Considering an ideal (100%) internal quantum efficiency (i.e., that each absorbed photon generates charge carriers that are then separated and collected at the cell contacts) one can determine an optical photocurrent density (J_{ph}) by integrating the absorption in the PV layer for the defined range, convoluted with the AM1.5 solar spectrum ($I_{\text{AM1.5}}$ in $\text{W m}^{-2} \text{ m}^{-1}$)^[3]

$$J_{\text{ph}} = e \int_{350 \text{ nm}}^{1200 \text{ nm}} \frac{\lambda}{hc} \text{Abs}(\lambda) I_{\text{AM1.5}}(\lambda) d\lambda \quad (1)$$

where e denotes the electron elementary charge, λ the Planck’s constant, and c the speed of light in vacuum. The optical photocurrent is typically used for comparison in literature as it neglects any electrical losses, so it defines the upper limit of the short-circuit current density (J_{SC}) of a solar cell.

Spectrophotometry was also used to determine the equivalent film thickness of the deposited TiO₂ material, after the mask infiltration step, by measuring the T_T spectra of glass samples subjected to the TiO₂ sputtering process. To confirm the sputtered TiO₂ thickness, the 1D Scattering Matrix Method was employed to analytically fit such T_T spectra with the simulated spectra of flat layers.

Photovoltaic Response: The pIBCSCs I–V measurements were performed using a LED-based Sun Simulator (Oriol VeraSol LSH-7520), supplying a 1-Sun illumination certified AAA in a 51 × 51 mm² area. Angular measurements were taken by adapting the sample holder with a goniometer. EQE measurements were performed using a Newport QuantX-300 system, between 350 and 1200 nm and with a 10 nm step.

Supporting Information

Supporting Information is available from the Wiley Online Library or from the author.

Acknowledgements

This work received funding from the FCT (Fundação para a Ciência e Tecnologia, I.P.) under the projects LA/P/0037/2020, UIDP/50025/2020 and UIDB/50025/2020 of the Associate Laboratory Institute of Nanostructures, Nanomodeling, and Nanofabrication—i3N, and by the projects TACIT (PTDC/NAN-OPT/28837/2017) and FlexSolar (PTDC/CTM-REF/1008/2020). The authors also acknowledge the support of the H2020 Solar-ERANET program, which funded the development of the IBC cells within the framework of the BOBTANDEM project. The work was also funded by the European Union's Horizon 2020 research and innovation program under the project Synergy (H2020-Widespread-2020-5, CSA), proposal n° 952169. M.A. and J.B. acknowledge funding by FCT-MCTES through the grants SFRH/BD/148078/2019 and BD/14557/2022, respectively.

Conflict Of Interest

The authors declare no conflict of interest

Data Availability Statement

The data that support the findings of this study are available from the corresponding author upon reasonable request.

Keywords

crystalline silicon solar cells, light management, photonic nanostructured coatings, photovoltaics

Received: February 3, 2023

Revised: March 15, 2023

Published online:

- [1] O. Sanchez-Sobrado, M. J. Mendes, T. Mateus, J. Costa, D. Nunes, H. Águas, E. Fortunato, R. Martins, *Sol. Energy* **2020**, 196, 92.
- [2] M. J. Mendes, S. Haque, O. Sanchez-Sobrado, A. Araújo, H. Águas, E. Fortunato, R. Martins, *iScience* **2018**, 3, 238.
- [3] S. Haque, M. Alexandre, M. J. Mendes, H. Águas, E. Fortunato, R. Martins, *Appl. Mater. Today* **2020**, 20, 100720.

- [4] C. Haginoya, M. Ishibashi, K. Koike, *Appl. Phys. Lett.* **1997**, 71, 2934.
- [5] A. P. Amalathas, M. M. Alkaiis, *Micromachines* **2019**, 10, 619.
- [6] C. S. Schuster, I. Crupi, J. Halme, M. Koç, M. J. Mendes, I. M. Peters, S. Yercie, in *Handbook of Climate Change Mitigation and Adaptation*, Springer International Publishing, Springer, New York **2022**, pp. 1165–1248.
- [7] O. Sanchez-Sobrado, M. J. Mendes, S. Haque, T. Mateus, H. Águas, E. Fortunato, R. Martinse, *J. Mater. Chem.* **2019**, 7, 6456.
- [8] S. Haque, M. J. Mendes, O. Sanchez-Sobrado, H. Águas, E. Fortunato, Martins R., *Nano Energy* **2019**, 59, 91.
- [9] O. Sanchez-Sobrado, M. J. Mendes, S. Haque, T. Mateus, A. Araujo, H. Águas, E. Fortunato, R. Martins, *J. Mater. Chem.* **2017**, 5, 6852.
- [10] A. R. Pascoe, S. Meyer, W. Huang, W. Li, I. Benesper, N. W. Duffy, L. Spiccia, U. Bach, Y. B. Cheng, *Adv. Funct. Mater.* **2016**, 26, 1278.
- [11] L. Zheng, Y. Ma, S. Chu, S. Wang, B. Qu, L. Xiao, Z. Chen, Q. Gong, Z. Wuc, X. Hou, *Nanoscale* **2014**, 6, 8171.
- [12] P. Tockhorn, J. Sutter, A. Cruz, P. Wagner, K. Jäger, D. Yoo, F. Lang, M. Grischek, B. Li, J. Li, O. Shargaieva, E. Unger, A. Al-Ashouri, E. Köhnen, M. Stolterfoht, D. Neher, R. Schlatmann, B. Rech, B. Stannowski, S. Albrecht, C. Becker, *Nat. Nanotechnol.* **2022**, 17, 1214.
- [13] M. J. Mendes, O. Sanchez-Sobrado, S. Haque, T. Mateus, H. Águas, E. Fortunato, R. Martins, *Wave-Optical Front Structures on Silicon and Perovskite Thin-Film Solar Cells*, **2019**.
- [14] M. J. Mendes, A. Araújo, A. Vicente, H. Águas, I. Ferreira, E. Fortunato, R. Martins, *Nano Energy* **2016**, 26, 286.
- [15] K. Li, S. Haque, A. Martins, E. Fortunato, R. Martins, M. J. Mendes, C. S. Schuster, *Optica* **2020**, 7, 1377.
- [16] M. J. Mendes, I. Tóbiás, A. Martí, A. Luque, *Opt. Express* **2011**, 19, 16207.
- [17] Y. Lei, Y. Li, Z. Jin, *Energy Rev.* **2022**, 1, 100003.
- [18] C. S. Schuster, S. Morawiec, M. J. Mendes, M. Patrini, E. R. Martins, L. Lewis, I. Crupi, T. F. Krauss, *Optica* **2015**, 2, 194.
- [19] S. Morawiec, J. Holovský, M. J. Mendes, M. Müller, K. Ganzerová, A. Vetushka, M. Ledinsky, F. Priolo, A. Fefjar, I. Crupi, *Sci. Rep.* **2016**, 6, 22481.
- [20] L. Hong, H. Yao, Z. Wu, Y. Cui, T. Zhang, Y. Xu, R. Yu, Q. Liao, B. Gao, K. Xian, H. Y. Woo, Z. Ge, J. Hou, *Adv. Mater.* **2019**, 31, 1903441.
- [21] T. Glinsner, P. Lindner, M. Mühlberger, I. Bergmair, R. Schöftner, K. Hingerl, *J. Vac. Sci. Technol., B: Microelectron. Nanometer Struct.—Process., Meas., Phenom.* **2007**, 25, 2337.
- [22] N. Pourdavoud, S. Wang, A. Mayer, T. Hu, Y. Chen, A. Marianovich, W. Kowalsky, R. Heiderhoff, H. C. Scheer, T. Riedl, *Adv. Mater.* **2017**, 29, 1605003.
- [23] S. Y. Chou, P. R. Krauss, P. J. Renstrom, *Science* **2013**, 272, 85.
- [24] Y. Yu, Zhang G. in *Colloidal Lithography: Updates in Advanced Lithography* (Ed. S. Hosaka), IntechOpen, Rijeka, Croatia **2013**, pp. 3–34.
- [25] R. D. Oliveira, A. Mouquinho, P. Centeno, M. Alexandre, S. Haque, R. Martins, E. Fortunato, H. Águas, M. J. Mendes, *Nanomaterials* **2021**, 11, 1665.
- [26] J. Chen, P. Dong, D. Di, C. Wang, H. Wang, J. Wang, X. Wu, *Appl. Surf. Sci.* **2013**, 270, 6.
- [27] T. Kohoutek, M. Parchine, M. Bardosova, H. Fudouzi, Pemble M., *Opt. Mater. Express* **2018**, 8, 960.
- [28] P. Centeno, M. F. Alexandre, M. Chapa, J. Pinto, J. Deuermeier, T. Mateus, E. Fortunato, R. Martins, H. Águas, M. J. Mendes, *Adv. Mater. Interfaces* **2020**, 7, 2070084.
- [29] J. L. N. Boane, P. Centeno, A. Mouquinho, M. Alexandre, T. Calmeiro, E. Fortunato, R. Martins, M. J. Mendes, H. Águas, *Micro* **2021**, 1, 215.
- [30] E. M. Akinoglu, A. J. Morfa, M. Giersig, *Langmuir* **2014**, 30, 12354.
- [31] A. Bazzola, M. Liscidini, L. C. Andreani, *Prog. Photovoltaics* **2012**, 20, 442.

- [32] L. C. Andreani, A. Bozzola, P. Kowalczewski, Liscidini M., *Sol. Energy Mater. Sol. Cells* **2015**, 135, 78.
- [33] A. Ingenito, O. Isabella, M. Zeman, *IEEE J. Photovoltaics* **2013**, 6, 1869.
- [34] A. Ingenito, O. Isabella, M. Zeman, *ACS Photonics* **2014**, 1, 270.
- [35] G. Torrisi, J. S. Luis, O. Sanchez-Sobrado, R. Raciti, M. J. Mendes, H. Águas, E. Fortunato, R. Martins, A. Terrasi, *Sol. Energy Mater. Sol. Cells* **2019**, 197, 7.
- [36] X. H. Li, P. C. Li, D. Z. Hu, D. M. Schaadt, E. T. Yu, *J. Appl. Phys.* **2013**, 114, 044310.
- [37] R. Kopecek, J. Libal, J. Lossen, V. D. Mihailetchi, H. Chu, C. Peter, F. Buchholz, E. Wefringhaus, A. Halm, J. Ma, L. Jianda, G. Yonggang, Q. Xiaoyong, W. Xiang, D. Peng, in *47th IEEE Photovoltaic Specialists Conf. (PVSC)*, IEEE, Piscataway, NJ **2020**, pp. 1008–1012.